CHAPTER 6

RESULT AND DICUSSION

In **Section 5.1** of **Chapter 5**, the event selections for long-lived neutral hadrons in the final states candidates found in the calorimeter of the ZEUS detector were described. The cuts applied on potential candidates for K_L^0, K_S^0, n, γ, e particles to narrow down to the most probable ones were carried out, to reconstruct the invariant mass of light unflavored meson $\phi(1020)$ through $\phi(1020) \rightarrow K_L^0 K_S^0$ channel and baryon Λ through $\Lambda \rightarrow n\pi^0$ channel, and its associated kinematics variables as described in **Chapter 3**.

Selection criteria for electrons scattered from the electron-proton collision were also given in **Section 5.3.1** of **Chapter 5** to find associations between the scattered electrons and the particles $\phi(1020)$ produced during the interaction. The selection criteria for photons scattered of from the scattered electron were also given. This category of photons was different from the ones originating from $\pi^0 \rightarrow \gamma\gamma$ decay through $\Lambda \rightarrow n\pi^0$ channel.

In this chapter, we present the results from cuts applied from **Chapter 5**, including the reconstructed variables associated with $\phi(1020) \rightarrow K_L^0 K_S^0$ as given in **Section 6.1)**, and $\Lambda \rightarrow n\pi^0$ decay channels given in **Section 6.2**.

6. 1 Reconstruction of $\phi(1020)$ mass from $\phi(1020) \rightarrow K_L^0 K_S^0$ channel

In **Section 5.2**, the selection criteria for candidates long lived neutral hadrons reaching the hadronic calorimeter of the ZEUS detector was given. In the following sections, the results from event selections of K_L^0 and K_S^0 candidates were given, with the former from the ZEUS Unidentified Flow Objects (ZUFOs) not associated with any tracks, while the latter from V0lite entries of $\pi^+\pi^-$ candidates for the reconstruction of K_S^0 through $K_S^0 \rightarrow \pi^+\pi^-$ decay channel. The potential $\phi(1020)$ candidates were constructed from the K_L^0 and K_S^0 candidates from decay channel $\phi(1020) \rightarrow K_L^0 K_S^0$ using the invariant mass $m(\phi(1020)) \rightarrow m(K_L^0\ K_S^0)$.

The results of the reconstructed scattered electrons $e(k')$ from $e(k)\ p(P) \rightarrow e(k')\ p(P')\ X\gamma$ interaction are also given the following section.

In this section, the result from grand reprocessing Monte Carlo data from Ariadne simulation data (Ariadne067p_GR) was used with the results given and discussed in the following sections.

6.1.1 Reconstruction of K_L^0 kinematic variables

In this thesis, the reconstruction of kinematic variables for K_L^0 was based on the energy of ZEUS Unidentified Flow Objects (ZUFOs) in hadronic calorimeter that was not associated with any tracks and identified as neutral energy. Conventionally, the ZUFOs energy tracks were determined by assuming the associated particles were pions [11].

Thus the reconstruction of neutral ZUFO object K_L^0 were limited to only four variables, i.e. firstly the of azimuthal and polar angles of the K_L^0 candidates from the ZUFOs momenta as given in **Equations (2.14)** and **(2.15)** of **Section 2.9** in **Chapter 2** of this thesis, secondly the energy zufo(4,Nzufos) of object-i in the ZUFOs four-momenta, thirdly the CAL energy zufoEcal(Nzufos) and finally the CAL EMC energy zufoEemc(Nzufos).

The following results were reconstructed based on the kinematic variables as described in **Section 2.9** in **Chapter 2.**

6.1.2 Background cuts

Figure 6.1a shows slight "bump" shape on the plot of energy of potential K_L^0 candidates (solid line) after undergoing selections as given in **Section 5.1**, as compared with the background signal (dash line) i.e. when the ratio of electromagnetic to hadronic energy of potential K_L^0 candidates was less than 1 % .To eliminate the background signal, the background was fitted with function $e^{a+b*zufo(4,i)}$ (refer to **Figure 6.1b**, with *a* and *b* constants and Zufo(4,i) as the energy of object-*i*) and later subtracted from the solid line **Figure 6.1a.**

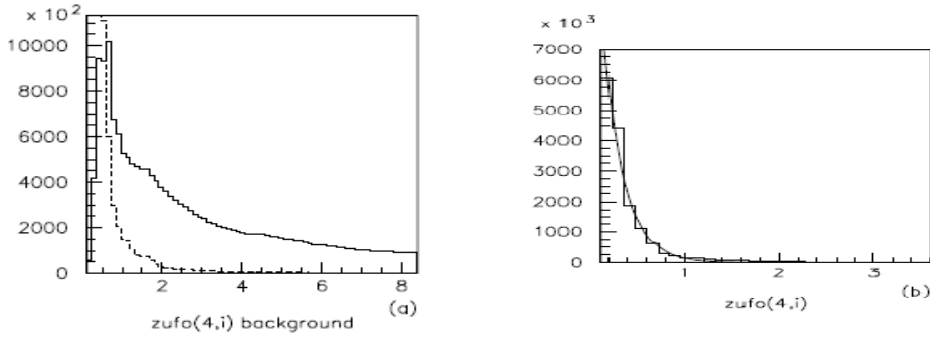

Figure 6.1a Comparison of ZUFOs energy $zufo(4,i)$ for object-*i* not associated with any track (solid line) against its background signal (dash line); (b) the background signal is curve fitted using function $e^{(a+b*zufo(4,i))}$ and is then used to isolate the ZUFOs energy of K_L^0 candidates from its background signal.

6.1.3 The four-momenta of K_L^0 candidates

In **Section 2.9** of this thesis, the kinematic variables of the ZUFO objects in the calorimeter of the ZEUS detector were described, with the momentum components in x, y, z direction, in terms of energy E azimuthal angle θ and polar angle ϕ, as given in **Equations (2.17), (2.18)** and **(2.9)**.

In **Figure 6.2**, the four-momenta of the hadronic ZUFOs momentum that was not associated with any tracks is given. **Figure 6.2(a)** shows the energy of potential K_L^0 candidates after undergoing background cut as described in **Section 6.1.1.1,** peak at 5GeV. The energy gap around 10GeV in **Figure 6.2(a)** might due to the supercrack i.e. a gap between the RCAL and BCAL region in the ZEUS detector.

Of the four-components, the x, y and z momentum components were used only to calculate cosine polar angle $\cos\theta$ and cosine azimuthal angle $\cos\phi$ of K_L^0, as candidates as the ZUFOs energy tracks were determined by assuming the associated particles were pions [11].

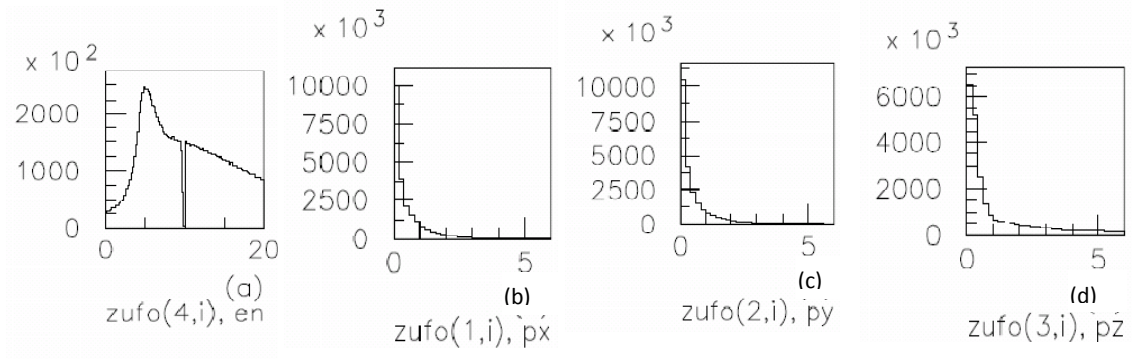

Figure 6.2 The four-momenta from ZUFOs entry for object-i not associated with any track (a) energy (GeV) of K_L^0 candidates and its associated momentum components (in GeV) (b) in x-direction (c) in y-direction (d) in z-direction assuming the particles as pions.

Figure 6.3(a) shows the measured cosine azimuthal angle $\cos\phi$ of K_L^0 candidates with the maxima appears to be at ~ 1 (0^0) and 0.75 (41^0). **Figure 6.3(b)** shows $\cos\phi$ of K_L^0 candidates, obtained from Monte Carlo simulation, with the momentum matched against its measured value. Both **Figure 6.3(a)** and **Figure 6.3(b)** showed similar trend but in the former there is additional peak at 0.75 (41^0).

Figure 6.4 shows cosine polar angles of K_L^0 candidates with $\cos\phi$ seemed to be oscillating with peaks at 0.15 (81^0), 0.35 (69^0), 0.575 (55^0), 0.725 (43.5^0), 0.65 (49^0). The effect in the latter could b attributed to the calorimeter segmentation of the calorimeters into modules and towers with front face of $25cm \times 21cm$.

The energy component as given in **Figure 6.2(a)** and the azimuthal from **Figure 6.3(a)** and polar angles as in **Figure 6.4** would be later used to reconstruct of kinematic variables of K_L^0 with the results as given in the following sections.

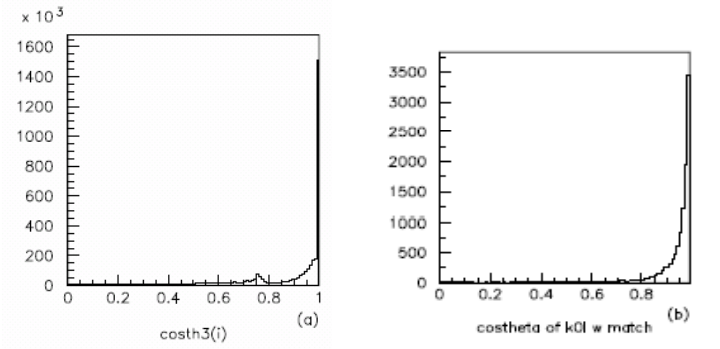

Figure 6.3 Cosine polar angles of K_L^0 candidates (a) measured $\cos\theta$ and (b) $\cos\theta$ from Monte Carlo simulation

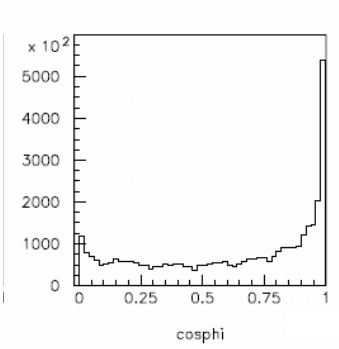

Figure 6.4 Azimuthal angles $\cos\phi$ of K_L^0 candidates

Figure 6.5 shows **,** the momentum of K_L^0 candidates calculated using **Equations (2.17), (2.18)** and **(2.19)** (of **Section 2.9 in Chapter 2),** assuming that neural hadron dissipated its energy in the same manner as photon and, using event selections as given in **Section 5.1 of Chapter 5**. The momentum of K_L^0 candidates in **Figure 6.5(a)** shows a maximum at 6GeV, similarly with the z-component in **Figure 6.5 (d),** as compared with the x and y-components. This indicates that the tendency of movement of K_L^0 candidates is more towards the front region of the calorimeter than the barrel region, and in contrast to **Figure 6.2(d)** that indicate significant transverse momentum from the ZUFOs object-i not associated with any track was treated as a pion.

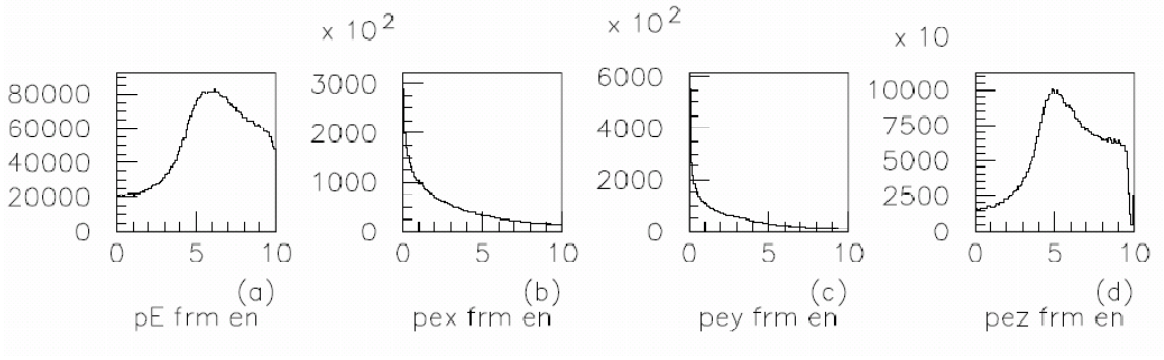

Figure 6.5 Reconstructed momentum distribution of K_L^0 candidates (a) momentum of K_L^0 candidates (b) momentum in x-direction (c) momentum in y-direction (d) momentum in z-direction

6.1.4 Kinematic variables of K_L^0

Figure 6.6 gives the transverse properties of K_L^0 candidates, with **Figure 6.6(a)** showing the transverse energy of the candidates, **Figure 6.6(b)** the transverse momentum of K_L^0 candidates, and in **Figure 6.6(c)** the $\delta_i = E_i - p_{zi}$ for K_L^0 candidates.

From **Figure 6.6c**, it appears that difference between the energy of K_L^0 candidates and its momentum in the z-direction is small. In **Figure 6.6a,** the transverse energy peak of K_L^0 candidates at about 0.5GeV, while **Figure 6.6b** shows the almost linear transverse momentum of the K_L^0 candidates.

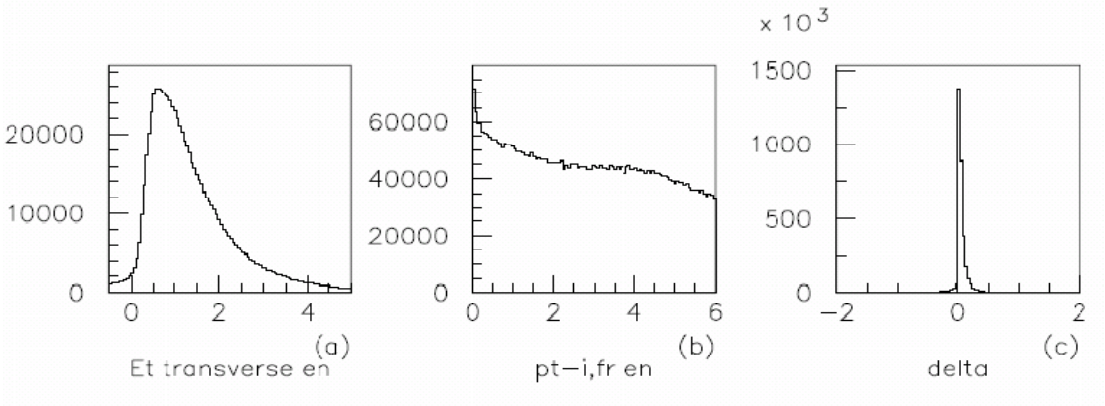

Figure 6.6 Transverse properties of K_L^0 candidates: (a) transverse energy (in GeV) (b) transverse momentum (in GeV) (c) $\delta_i = E_i - p_{zi}$ (in GeV)

Figure 6.7 shows the rapidity *y* and pseudorapidity η of K_L^0 candidates. In **Figure 6.7a,** the entries are given only in the forward region of the detector, while in **Figure 6.7b** the entries are given in both the forward and rear region of the detector, with $-2 < \eta < 2$ in barrel direction of the ZEUS detector when the Lorentz transformation in almost linear, while outside this region (close to the beam pipe in the forward and rear region of the detector) η values would most probably include reactions near the beampipe region. In both **Figure 6.7a** and **Figure 6.7b,** the highest entries is at $\eta \sim 0.8$, indicating the production region of K_L^0 highest around this region.

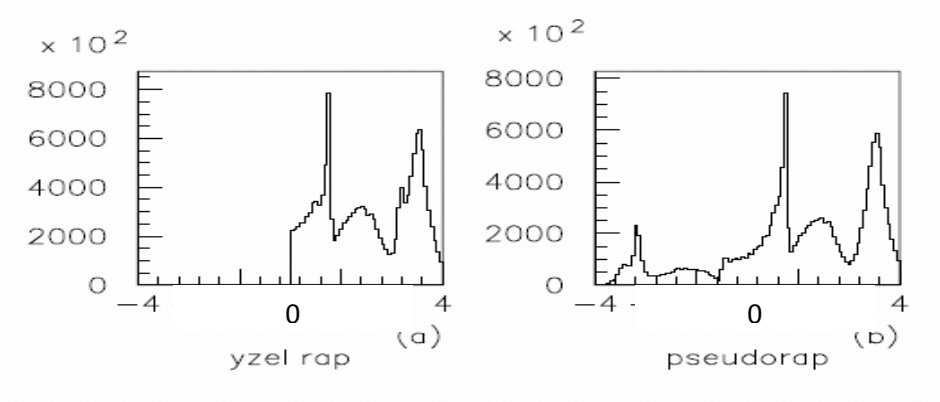

Figure 6.7 (a) Rapidity and (b) pseudorapidity of K_L^0 candidates

Figure 6.8a gives the momentum gain $Q^2 = -(k - k')^2$ from incoming electron during the DIS, showing Q^2 from the Jacquet-Blondel method to be in the range from 0 to 100GeV, as compared with **Figure 6.10d** (see the following **Section 6.15**) that shows $Q^2 = -(k - k')^2$ to be in slightly higher range of 0 to 150GeV from the electron method. For relatively low Q^2, the electron method is more preferable for its higher resolution [28] as given in **Section 2.9.1** of **Chapter 2**.

Figure 6.6c shows fraction $x_{JB} = \frac{Q^2}{sy_{JB}}$ of transferred proton momentum to a struck quark from Jacquet-Blondel method, while **Figure 6.6 (d)** gives the centre-of-mass $W_{JB} = \sqrt{y_{JB}\, s}$, for the intermediate boson-proton interaction during DIS, with peak at about 25GeV.

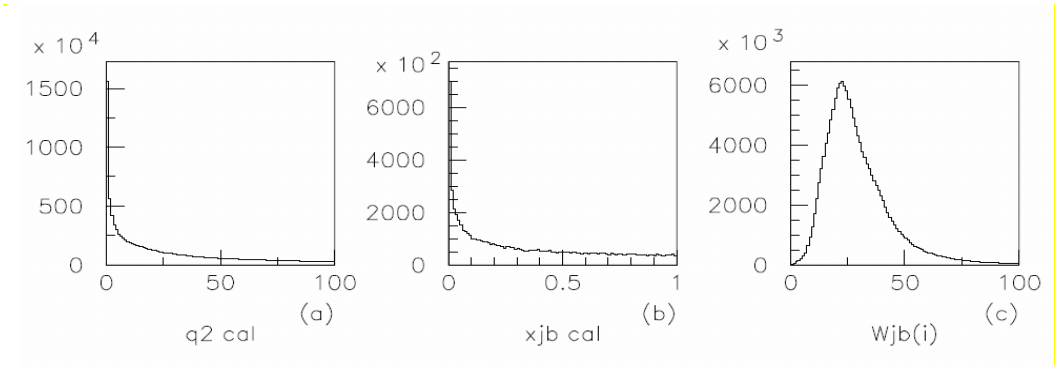

Figure 6.8 Properties of reconstructed K_L^0 reconstructed candidates (a) Momentum gain from incoming electron $Q^2 = -(k - k')^2$;(b) $x_{JB} = \frac{Q^2}{sy_{JB}}$ as fraction of transferred proton momentum to a struck quark ;(c) centre-of-mass $W_{JB} = \sqrt{y_{JB}\, s}$, for the intermediate boson-proton

6.1.5 Reconstruction of Scattered electrons in $e(k)\ p(P) \rightarrow e'(k')\ p'(P')\ X\gamma$ interaction

In the Deep Inelastic Scattering (DIS), the electron remnant $e'(k')$ from the electron-proton collision carries with it the leftover of momentum transferred to the real photon during the DIS to produce $\phi(1020)$.

Figure 6.9 gives the reconstructed momentum of the scattered electron $e'(k')$ candidates from DIS interaction, using ZUFOs associated with charge tracks in EMC of ZEUS detector, with event selection as given in **Section 5.3.1** of **Chapter 5**. The scattered electrons from DIS interaction were selected to be the rear region i.e. 1.2 rad and 3.1 rad of the calorimeter.

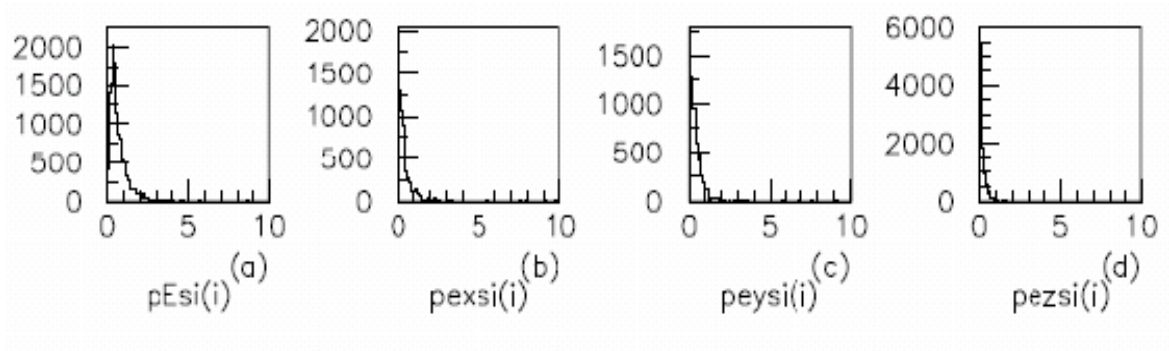

Figure 6.9 Reconstructed momentum of scattered electron candidates from DIS (a) momentum of scattered electron with (b) in x-direction; (b) y-direction (c) in z-direction, using ZUFOs charge tracks in EMC of ZEUS detector

In **Figure 6.10a** the polar angle θ_e at ~ 1.3 radian shows that the remnant electron $e'(k')$ was in the rear region of the calorimeter. **Figure 6.10b** shows the azimuthal angle ϕ_e of scattered electron, while **Figure 6.10c** the energy remnant the scattered electron $e'(k')$ after DIS the to be in the range of 0 to 2GeV.

Figure 6.10d, shows the virtual photon gain $Q^2 = -(k-k')^2$ to be in the range of 0 to 150GeV using the electron method, , indicating "hard" interaction involved during DIS.This gain is comparable to the Q^2 from the Jacquet-Blondel method as given in **Figure 6.8(a)** of **Section 6.1.4,** and is higher in resolution for relatively low Q^2.

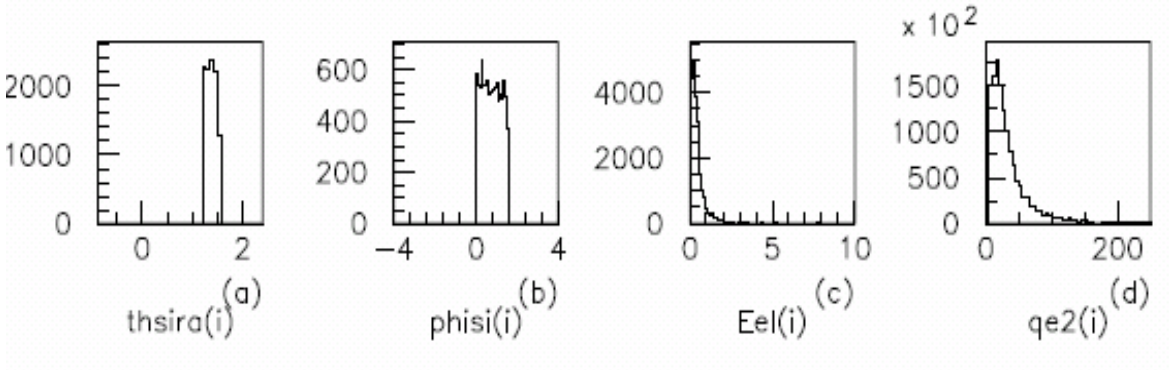

Figure 6.10 Properties of reconstructed scattered electron candidates from DIS (a) polar angle θ in radian; (b) azimutal angle ϕ in radian (c) energy (GeV); (d) virtual photon gain $Q^2 = -(k-k')^2$, using ZUFOs charge tracks in EMC of ZEUS detector

Figure 6.11 shows two dimensional plot of energy (from **Figure 10(b)**) of remnant electron $e'(k')$ from DIS (in direction 1.3 radian) versus the photon momentum gain $Q^2 = -(k-k')^2$. The linear correlation between both variable in this plot indicates the linear dependency of Q^2 on the scattered electron's energy or as $Q_i^2 = 2E_{ei}E_{ei}^{'}(1+\cos\theta_{ei})$ from the electron method as given in **Equation (2.30)** in **Section 2.9.1**

In **Figure 6.12**, the two dimensional plot of $Q^2 = -(k-k')^2$ versus centre-of-mass $W_{JB} = \sqrt{y_{JB}\, s}$ for the intermediate boson-proton W_{JB} shows that the photon momentum gain Q^2 dependency on W_{JB} is almost cluster-like, with the highest around (W_{JB}, Q^2) ~ (20GeV, 15GeV^2)

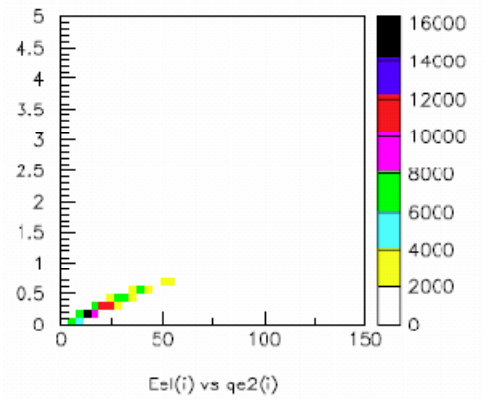

Figure 6.11 Two dimensional plot of energy (GeV) of scattered electron candidates from DIS vs. $Q^2 = -(k-k')^2$.(GeV)^2

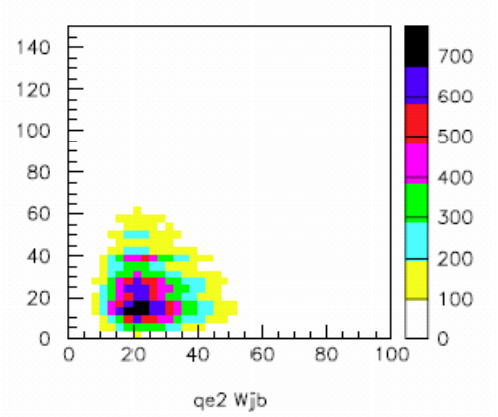

Figure 6.12 Two dimensional plot of $Q^2 = -(k-k')^2$ vs centre-of-mass $W_{JB} = \sqrt{y_{JB}\, s}$ for the intermediate boson-proton

6.1.6 Reconstructed mass of K_L^0

In the deep inelastic scattering (DIS) during electron-proton collision, the virtual photons emitted by the incoming electron behave in point-like manner to fluctuate into the proton via an exchange of pomeron to produce vector meson ϕ that decays into K_L^0 and K_S^0.

In **Section 2.9** of this thesis, the kinematic variable of ZUFO object-i in the calorimeter of the ZEUS detector has been described. By assuming that neutral hadrons dissipate its energy in the same manner as photon (i.e. $E^2 = p^2$ [27]), **Equations (2.17), (2.18) and (2.19)** were used to approximate the momentum of neutral ZUFO object in the calorimeter of ZEUS detector.

In **Equation 2.22** of **Section 2.9**, the mass of neutral ZUFO object-*i* (assuming that neutral hadrons dissipated its energy in the same manner as photon), is approximated by,

$$mass_i = \sqrt{E_i^2 - (E_i \sin\theta_i \cos\phi_i)^2 - (E_i \sin\theta_i \sin\phi_i)^2 - (E_i \cos\theta_i)^2} \qquad (2.22)$$

However, the use of **Equations (2.17), (2.18), (2.19)** to estimate the four-momentum of hadrons in neutral and charge current (NCC) in the final state in the calorimeter of the ZEUS detector [17] and, to calculate the momentum of the scattered positron in a leading neutron in photoproduction [9] and the electron in diffractive DIS tagged with leading proton spectrometer [13] shows that the mass in approximated by **Equation (2.22)** would have significant value especially for neutral hadron in the final state.

In F**igure 6.13** invariant mass of K_L^0 candidates reconstructed from ZUFOs objects not associated with any track but forming islands of energy deposit in the calorimeter of the ZEUS detector, using the **Equation (2.22)**. **Figure 6.7(a)** shows the mass peak around 0.5GeV, which is in good agreement with the invariant K_L^0 mass of 0.498GeV [35].

From F**igure 6.13**, it can be observed that the width peak is quite wide. This is due to the limited variables available for K_L^0 candidate selection i.e. the polar angle θ of ZUFO object-*i*, the ZUFO object-*i* energy , the ZUFOs CAL energy and finally the CAL EMC energy for neutral ZUFOs objects in the calorimeter that were not associated with any track.

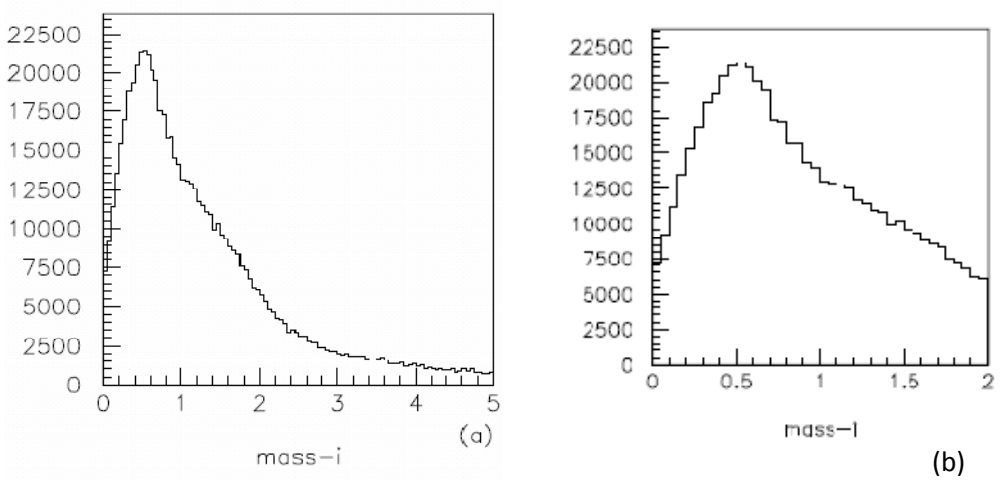

Figure 6.13 (a) Reconstructed mass in GeV of K_L^0 candidates, from ZUFO objects not associated with any tracks (b) an expansion of Figure (a) . The invariant mass of K^0 is 0.498GeV [35]

Figure 6.14 shows invariant mass of K_L^0 candidates with small standard deviation, indicating good statistical sample numbers,

Figure 6.14 gives standard deviation of invariant mass of K_L^0 candidates, showing small error for the reconstructed K_L^0 invariant mass. **Figure 6.15** gives comparison of mass of K_L^0 from Monte Carlo simulation (solid line) against the reconstructed mass (dash line) in GeV on log scale, showing good agreements between both simulated and reconstructed values.

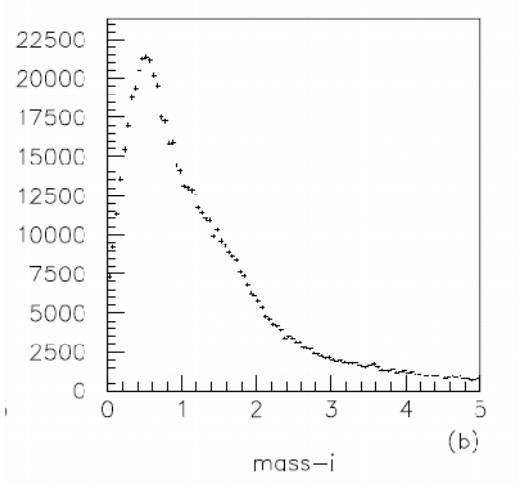

Figure 6.14 Reconstructed mass (in GeV) of K_L^0 candidates with errors. The invariant mass of K^0 is 0.498GeV

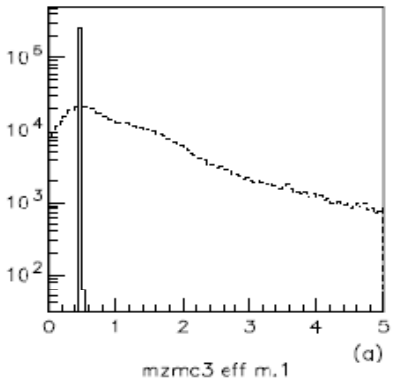

Figure 6.15 Comparison of mass of K_L^0 from Monte Carlo simulation (solid line) against reconstructed mass of K_L^0 candidates (dash line) in GeV on log scale.

Figure 6.16 gives two dimensional plot of mass versus $\cos\vartheta$ of K_L^0 at pseudorapidity $-2<\eta<2$, with ϑ as the polar angle of K_L^0, From this figure, it can be seen that the mass K_L^0 came from direction $\cos\vartheta$=0.95 or ϑ=18.2^0.

The pseudorapidity $-2<\eta<2$ gave Lorentz transformation of K_L^0 mass in the barrel direction of ZEUS calorimeter, where the mass transformation along the z-axis was invariant.

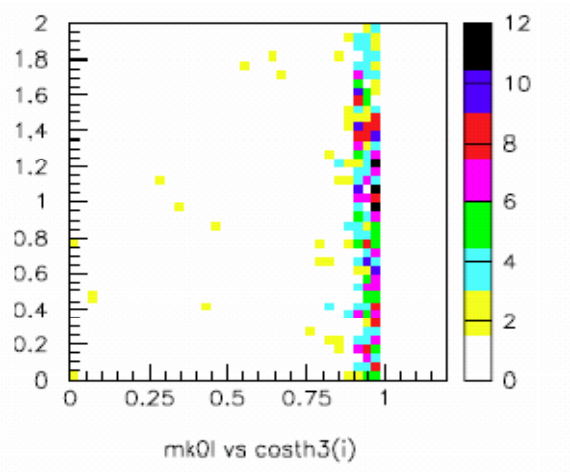

Figure 6.16 (a) Two dimensional plot of mass (GeV) vs $\cos\vartheta$ of K_L^0 at pseudorapidity $-2<\eta<2$ **(**ϑ **as the** polar angle of K_L^0)

6.1.6.1 Cross section of K_L^0

The differential cross section σ of the variable momentum p of K_L^0 candidates, calculated using Equation (5.6) of Section 5.7 in Chapter 5, using integrated luminosity (2006/2007) of 145.90pb^{-1} and branching ratio taken of 34.0% for $\phi(1020) \rightarrow K_L^0\ K_S^0$ decay channel.

Figure 6.17 (a) gives measured momentum of K_L^0 candidates with **Figure 6.17 (b)** giving the measured momentum of K_L^0 candidates that matched in magnitude and direction against the ones from generated from Monte Carlo, while **Figure 6.17 (c)** shows the corrected K_L^0 momentum, with the acceptance as given in **Figure 6.18 (c).**

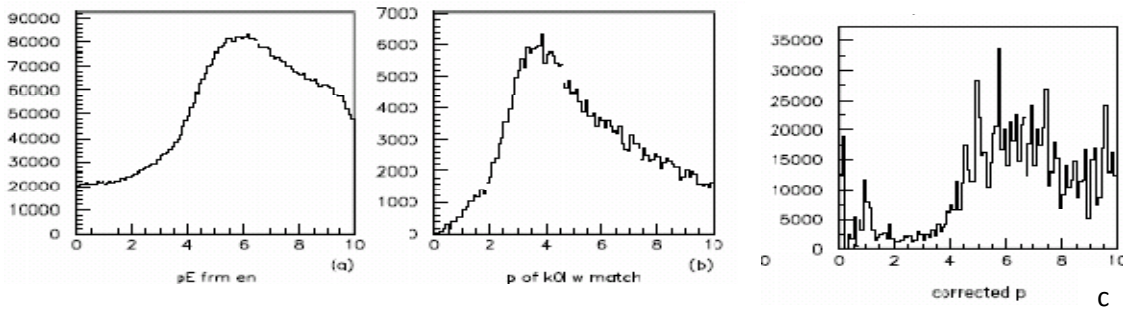

Figure 6.17 Comparison of momentum (in GeV) of K_L^0 candidates (a) measured (b) matched against the ones generated from Monte Carlo and matched against measured momentum; (c) corrected

Figure 6.18(a) and **(b)** give efficiency and the purity of the momentum of K_L^0 candidates with the former peak at ~4GeV while in the latter peak at ~ 5.5GeV. In **Figure 6.19**, the differential cross section with respect to momentum of K_L^0 is given with maximum ~5GeV.

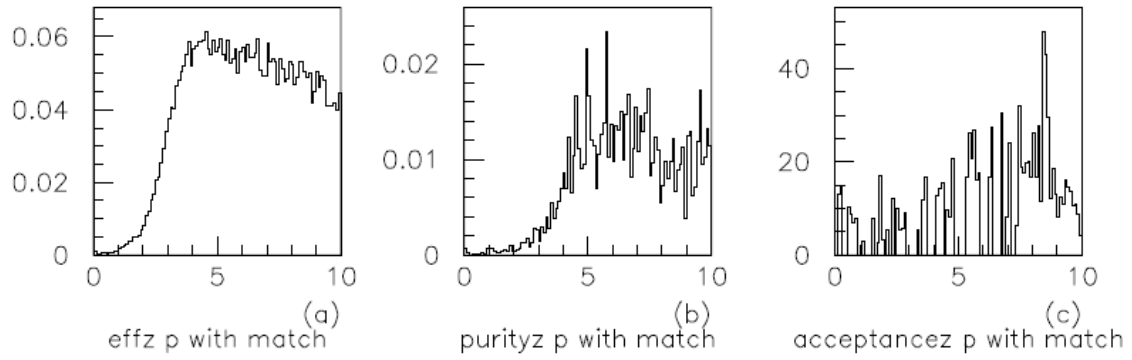

Figure 6.18 Comparison of (a) efficiency vs. energy (in GeV); (b) purity vs. energy (GeV); (c) acceptance vs. energy (GeV) of momentum of K_L^0 candidates

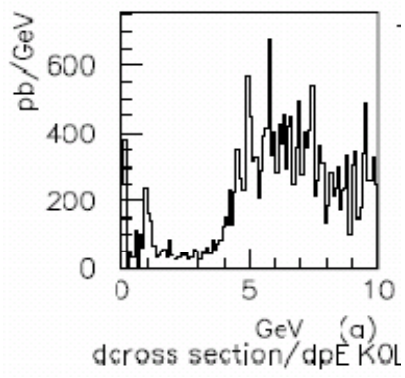

Figure 6.19 Differential cross section (in pb/GeV) of K_L^0 candidates with respect to its measured momentum vs. its energy (in GeV)

6.1.7 Reconstruction of K_S^0 momentum

Figure 6.24 shows the reconstructed momentum of K_S^0 candidates using selection criteria as given in **Section 5.2** of **Chapter 5** for lone hadron from the V0 entries that identified a pair of $\pi^+\pi^-$ potential candidates that decayed from a $K_s^0 \to \pi^+\pi^-$ channel. In **Figure 6.20a,** the momentum of momentum of K_S^0 from $K_s^0 \to \pi^+\pi^-$ channel is given, showing a peak ~1GeV, while **Figures 6.20b** to **6.20d** give the momentum components in the direction x, y and z respectively.

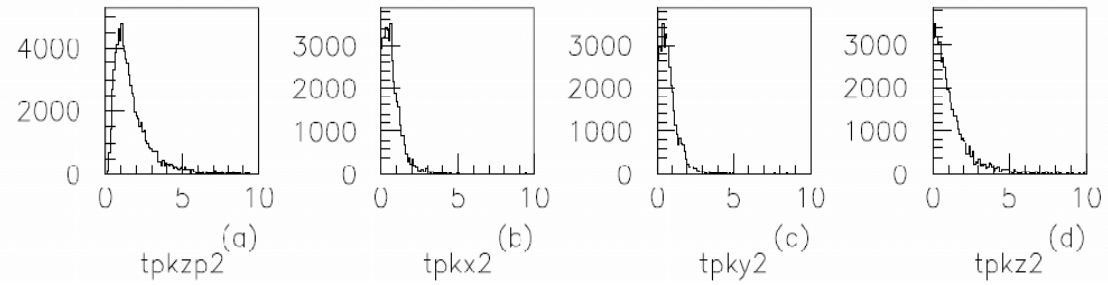

Figure 6.20 Reconstructed momentum (in GeV) of K_S^0 candidates (a) momentum of K_S^0 with (b) in x-direction; (b) y-direction (c) in z-direction

In **Figure 6.21,** two dimensional plot of mass (GeV) versus polar angle $\cos\vartheta$ of K_S^0 at pseudorapidity $-2 < \eta < 2$ is given, showing polar angle of K_S^0 at 18.2^0 $(Cos\theta = 0.95)$**,** which is in the same direction of K_L^0 as shown previously in **Figure 6.16a.**

These observations indicate that K_S^0 and K_L^0 may not be an exclusive ϕ decay as depicted in **Figure 2.11** of **Chapter 2** in this thesis.

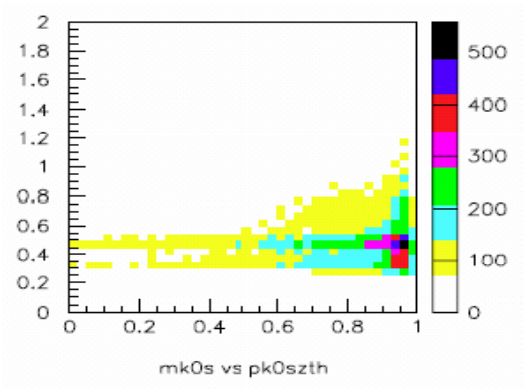

Figure 6.21 Two dimensional plot of mass (GeV) vs $\cos\vartheta$ of K_S^0 at pseudorapidity $-2 < \eta < 2$ **(**ϑ as the polar angle of K_S^0)

6.1.8 Reconstruction of $\phi(1020)$

In this section, the reconstruction of $\phi(1020)$ mass from the decay channel $\phi(1020) \rightarrow K_L^0 K_S^0$ i.e. $m(\phi(1020)) \rightarrow m(K_L^0\ K_S^0)$, was carried out by using the reconstructed mass of from K_L^0 from **Section 6.1.6** and the reconstructed mass of K_S^0 from $K_s^0 \rightarrow \pi^+\pi^-$ decay channel from lone hadron from the V0 entries of **Section 6.1.7**. The result is given in **Figure 6.22a**.

In **Figure 6.22 (a)** and **(b)**, the reconstruction of $\phi(1020)$ from $m(\phi(1020)) \rightarrow m(K_L^0\ K_S^0)$ shows a maximum entries of about 1300 at 1.05GeV, this is in good agreement with the invariant mass of 1.019 GeV [35]. The standard deviation of the reconstructed $\phi(1020)$ mass is small, as indicated by the error bars in the plot in **Figure 6.22c.** However, the limitation of event selection of K_L^0 candidates as described in **Section 6.1.6** contributed to the relatively wide width of the peak in **Figure 6.22a.**

For comparison purposes, the reconstructed masses of K_L^0 and K_S^0 are also given in **Figure 6.23a** and **Figure 6.23b,** while the reconstructed K_S^0 mass narrowed down to $abs(Mass(\pi^+\pi^-) - Mass(K_S^0)) < 0.02\ GeV/c^2$ as given **Section 5.2** of this thesis.

In **Figure 6.24 (a)**, comparison of reconstructed $\phi(1020)$ mass in GeV (dash line) with the mass from Monte Carlo simulation (solid line) is given, showing good agreements between both reconstructed and simulated values.

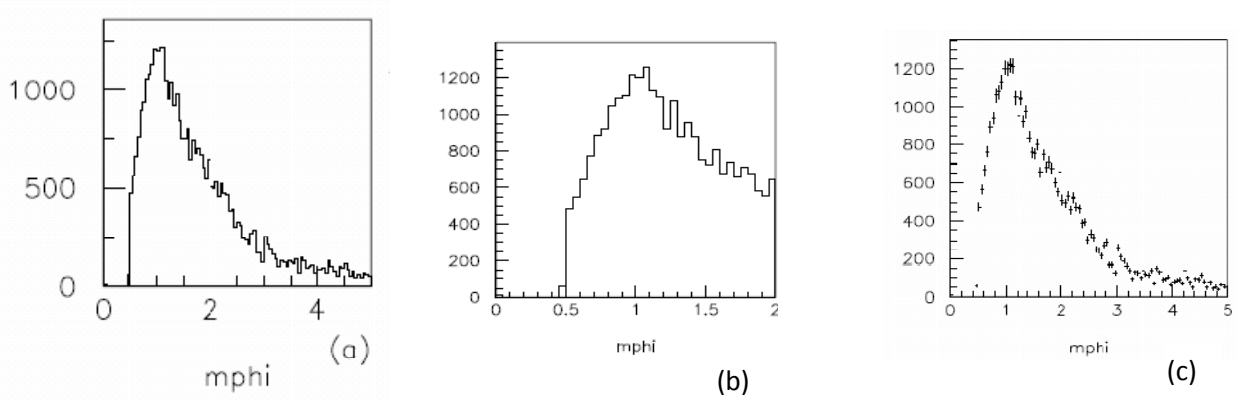

Figure 6.22 Reconstructed mass of $\phi(1020)$ from $\phi(1020) \rightarrow K_L^0 K_S^0$ channel (a) $\phi(1020)$ mass from $m(\phi(1020)) \rightarrow m(K_L^0\ K_S^0)$; (b) an expansion of Figure (a); (c) Statistical error of the reconstructed $\phi(1020)$ mass from $\phi(1020) \rightarrow K_L^0 K_S^0$ channel. The invariant mass of $\phi(1020)$ is 1.019 GeV [35]

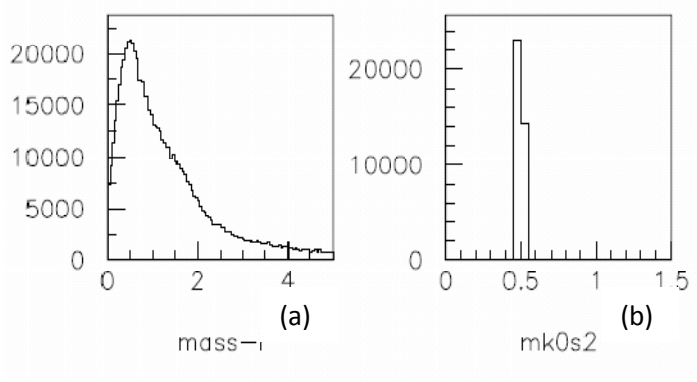

Figure 6.23 Reconstructed masses (in GeV) of (a) K_L^0 candidates using the ZUFOs entries; (b) mass K_S^0 candidates from V0 entries narrowed to $abs(Mass(\pi^+\pi^-) - Mass(K_S^0)) < 0.02$.

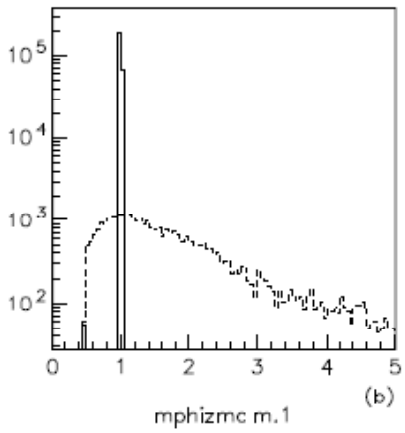

Figure 6.24 Comparison of mass of $\phi(1020)$ reconstructed mass in GeV (dash line) against its mass from Monte Carlo simulation (solid line)

The works by Chekanov et. al. (2001) on inclusive $\phi(1020)$ meson production in neutral deep inelastic scattering at HERA using $\phi(1020)$ reconstructed from $\phi(1020) \to K^+K^-$ channel in Breit frame with $10 < Q^2 < 100 GeV^2$ gave $\phi(1020)$ mass 1.016GeV with maximum ~ 4500 entries, which is comparable to the measured mass of $\phi(1020)$ **Figure 6.22** from $\phi(1020) \to K_L^0 K_S^0$ channel.

Measurements of $\phi(1020)$ using $\phi(1020) \to K^+K^-$ channel from $e^+e^- \to K_L^0 K_S^0$ process from heavy ion collisions by Abelev et. al. (2008) gave invariant mass of $\phi(1020)$ of 1.02GeV/c with $0.8 < p_T < 1.2 GeV/c$.

6.1.8.1 Cross section of $\phi(1020)$

Figure 6.25 compares momentum (in GeV) of $\phi(1020)$ candidates, with the **Figure 6.25a** giving the measured momentum ; (b) corrected; (c) simulated from Monte Carlo and matched against measured momentum (in GeV) of $\phi(1020)$ candidates, with **Figure 6.25a** showing the momentum maximum entries ~500. After correction, the entries gain by a factor of 4 as shown in **Figure 6.25b,** with the simulated momentum matched in magnitude and direction against measured momentum showing entries 20 times higher with maximum ~5GeV as in **Figure 6.25c**.

In **Figure 6.26,** the efficiency, purity and acceptance of momentum of $\phi(1020)$ candidates versus its energy (in GeV) are shown. The differential cross section σ with respect to the momentum p of $\phi(1020)$ candidates is given in **Figure 6.27**, calculated using a standard bin-by-bin correction is given in **Equation (6.1).**

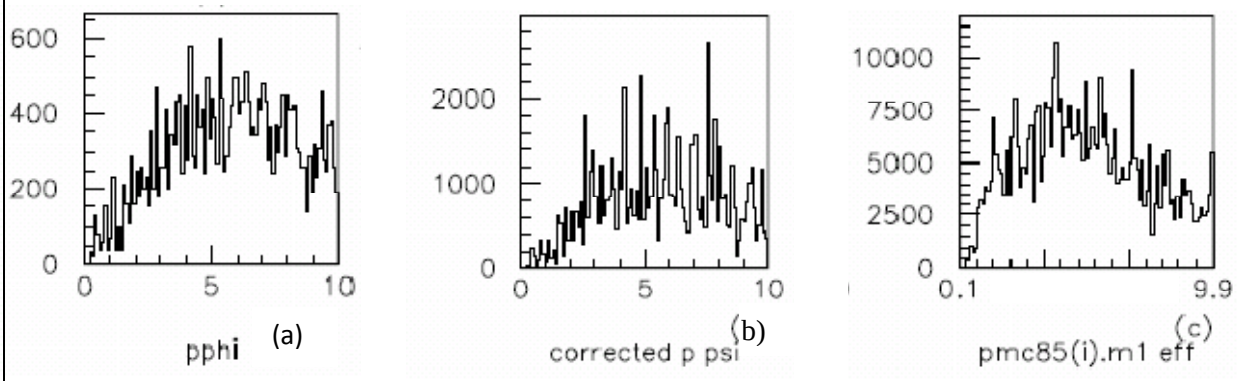

Figure 6.25 Comparison $\phi(1020)$ momentum (in GeV) (a) measured; (b) corrected; (c) simulated from Monte Carlo and matched in against measured momentum

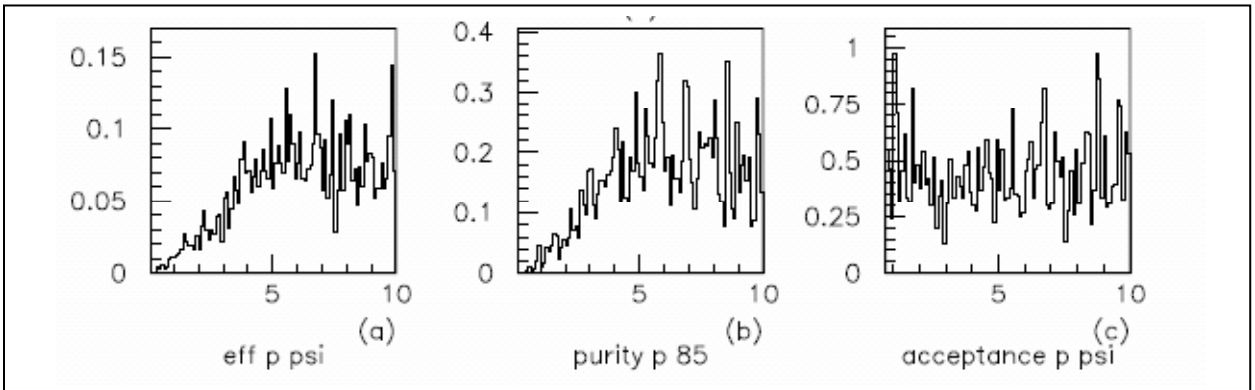

Figure 6.26 Comparison of (a) efficiency; (b) purity; (c) acceptance of momentum of $\phi(1020)$ candidates versus energy (in GeV)

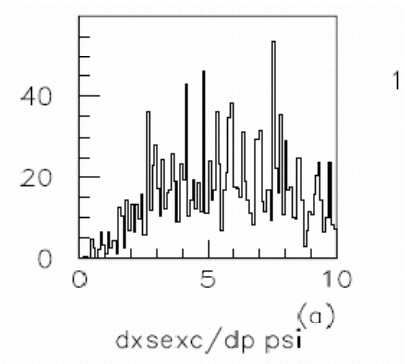

Figure 6.27 Differential cross section (in pb/GeV) of $\phi(1020)$ candidates with respect to its measured momentum vs its energy (in GeV)

6.1.8.2 Correlation of $\phi(1020)$ with polar angles with K_L^0 and K_S^0

In the exclusive ϕ production with decay channel $\phi \to K_L^0 K_S^0$, the momentum conservation requires that K_L^0 and K_S^0 to be in the opposite direction, as shown in **Figure 2.11** of **Chapter 2.** But **Figure 6.16** and **Figure 6.21** show that both K_L^0 and K_S^0 moving in the same direction at $\cos\vartheta = 0.95$ or $\theta = 18.2^0$, thus indicating the measured ϕ an inclusive event .

Figure 6.28 shows cosine azimuthal angle $\cos\vartheta$ of $\phi(1020)$ peaking at $\cos\vartheta = 0.7$ $(\theta = 45.6^0)$ and near $\cos\vartheta \sim 1$. **Figure 6.29** shows two dimensional plot of mass $\phi(1020)$ (GeV) versus $\cos\vartheta$ of K_L^0 of at pseudorapidity $-2 < \eta < 2$, while **Figure 6.30** shows the similar plot for mass $\phi(1020)$ (GeV) versus $\cos\vartheta$ of K_L^0.

In **Figure 6.29**, the peaks occur at azimuthal angle of K_L^0 at $\cos\vartheta$=0.75 and $\cos\vartheta$ =0.95 indicating possible correlation between $\phi(1020)$ and K_L^0 in the direction of $\cos\vartheta = 0.7$ $(\theta = 45.6^0)$.

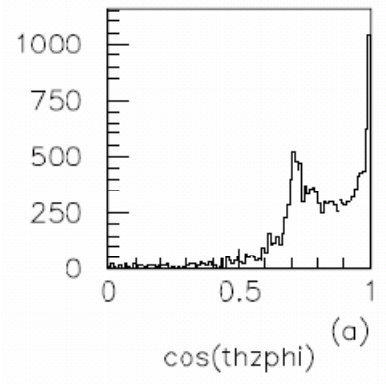

Figure 6.28 Cosine polar angle $\cos\vartheta$ of $\phi(1020)$

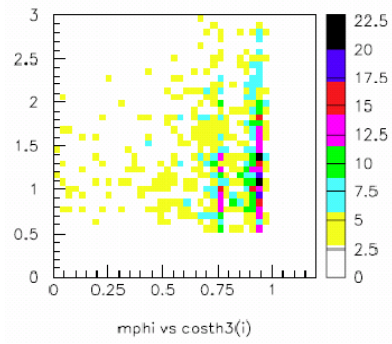

Figure 6.29 Two dimensional plot of mass $\phi(1020)$ (GeV) vs $\cos\vartheta$ of K_L^0 at pseudorapidity $-2 < \eta < 2$ (ϑ as the polar angle K_L^0)

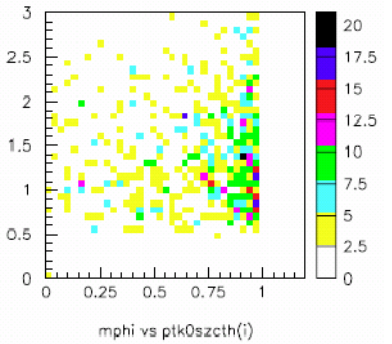

Figure 6.30 Two dimensional plot of mass $\phi(1020)$ (GeV) vs $\cos\vartheta$ of K_S^0 at pseudorapidity $-2 < \eta < 2$ (ϑ as the polar angle of K_S^0)

Figure 6.31 shows projection of K_L^0 mass (in GeV) versus $\phi(1020)$ mass (in GeV) using the ZUFOs method that uses islands of energies that was not associated with any track, while **Figure 6.32** shows projection of K_L^0 mass (in GeV) versus $\phi(1020)$ mass (in GeV) using the tracking method from CTD entries [27].

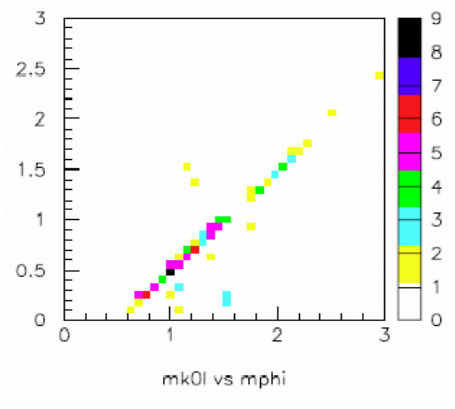

Figure 6.31 Two dimensional plot of K_L^0 mass (in GeV) vs. $\phi(1020)$ mass (in GeV)

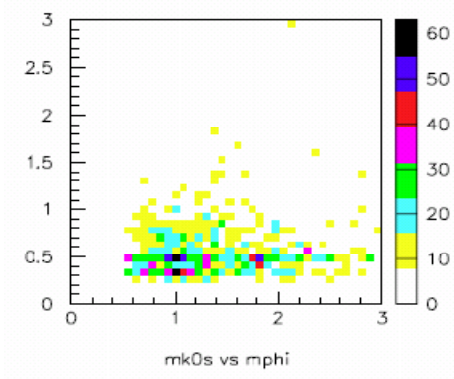

Figure 6.32 Two dimensional plot of K_S^0 mass (in GeV) vs. $\phi(1020)$ mass (in GeV)

6.2 Production of Λ from $\Lambda \to n\pi^0$ channel

In **Section 5.6**, the selections of n and $\gamma\gamma$ from π^0 decay and the reconstruction of Λ^0 mass from n and π^0 masses have been described. In this section, the result from these cuts that gave kinematic variables of n and $\gamma\gamma$, finally the reconstructed mass of Λ^0 from n and π^0 masses.

In this section, the result from grand reprocessing Monte Carlo from Pythia simulation data (DijetLF067p_GR**)** was used with the results given and discussed in the following sections.

6.2.2 Background cuts

As in **Section 6.1.2**, the background cuts was carried out energy plot after undergoing event selections as given in **Section 5.1,** with the background signal (dash line) i.e. when the ratio of electromagnetic to hadronic energy of potential neutron candidates was less than 1 % . **Figure 6.33** shows out energy plots of potential neutron candidates mixed with background (solid line) and the background alone (dash line). **Figure 6.33b** shows the background fitted with function $e^{a+b*zufo(4,i)}$ (a and b as constants and Zufo(4,i) as the energy of object-i) and later subtracted from mixed plot in **Figure 6.33a.**

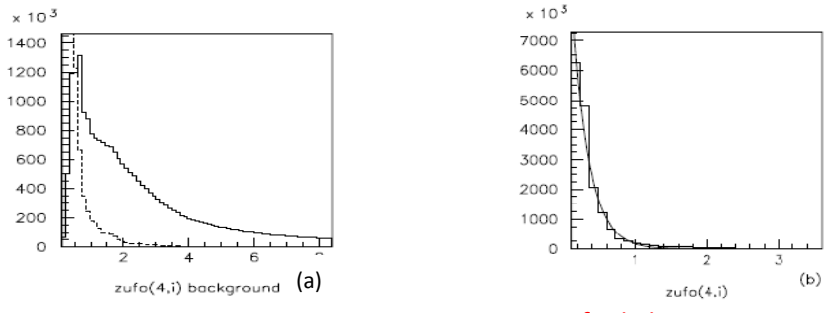

Figure 6.33 Comparison of ZUFOs energy $zufo(4,i)$ (in GeV) for object-i not associated with any track (solid line) against its background signal (dash line) for neutron candidates; (b) the background signal is curve fitted using function $e^{(a+b*zufo(4,i))}$ and is then used to isolate the ZUfOs energy of K_L^0 candidates from its background signal.

6.2.3 The four-momenta of neutron candidates

After background cut using the curve fit as given in **Figure 6.33 (b)**, the energy of the neutron candidates from ZUFOs object not associated with any track is given in **Figure 6.34(a)**, showing a peak at 6GeV. As with in **Section 6.1.3**, the momentum in x, y, z components as in **Figure 6.34(b), (c)** and **(d)** would only be used to calculate cosine polar angle $\cos\theta$ and cosine azimuthal angle $\cos\phi$ for neutron candidates as these values were calculated using pion mass.

was used with the results given and discussed in the following sections

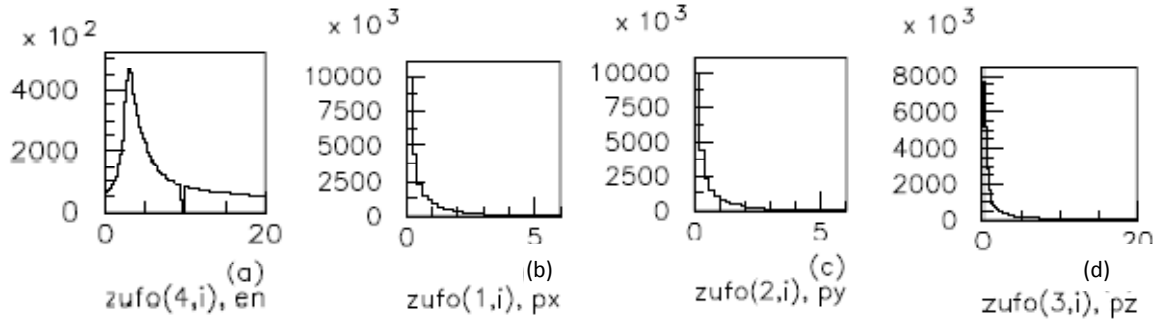

Figure 6.34 Four-momentum (in GeV) from ZUFOs entry for object-i not associated with any track used in neutron reconstruction (a) Energy component (b) x-component (c) y-component (d) z-component

In **Section 2.9** of this thesis, the kinematic variables of the ZUFO objects in the calorimeter of the ZEUS detector were described, with the momentum components in x, y, z direction, in terms of energy E azimuthal angle θ and polar angle ϕ, as given in **Equations (2.17), (2.18) and (2.9)**.

Figure 6.35 shows the momentum of neutron candidates from ZUFOs object-i that was not associated with any track in the calorimeter of the ZEUS detector, calculated using **Equations (2.17),(2.18)** and **(2.19)** after event selection as given in **Section 2.9** of **Chapter 2**. The neutron momentum in **Figure 6.35a** shows a peak at 3.5GeV while its z-component peaks at 3GeV **Figure 6.35d,** with no significant x and y components**.** This indicates the tendency of neutron candidates to move in the forward direction.

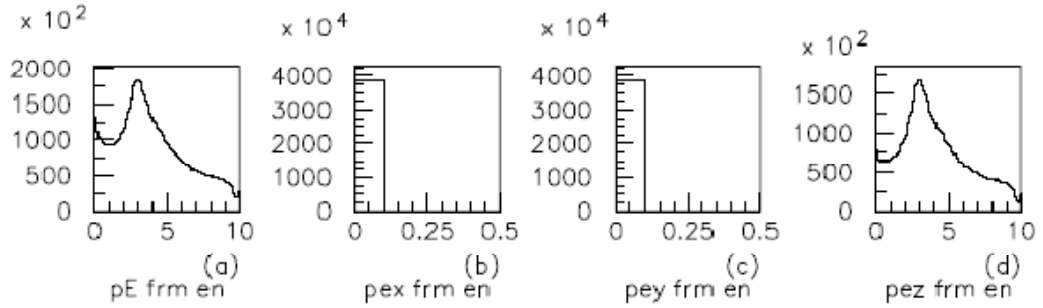

Figure 6.35 Reconstructed four-momentum (in GeV) of neutron candidates (a) Energy component (b) x-component (c) y-component (d) z-component

In **Figure 6.36a,** the measured cosine polar angle $\cos\theta$ of neutron candidates is given, with the maxima appears to be at ~ 1 (0^0) and 0.75 (41^0). **Figure 6.36b** shows $\cos\theta$ of neutron candidates from Monte Carlo simulation with the momentum matched against its measured value. Both **Figure 6.36a** and **Figure 6.36b** show similar trend but in the former there is additional peak at 0.75 (41^0).

As in **Section 6.1** of this chapter, energy component as given in **Figure 6.34a** and the polar angle from **Figure 6.36a** would be later used to reconstruct of kinematic variables of K_L^0 with the results as given in the following sections.

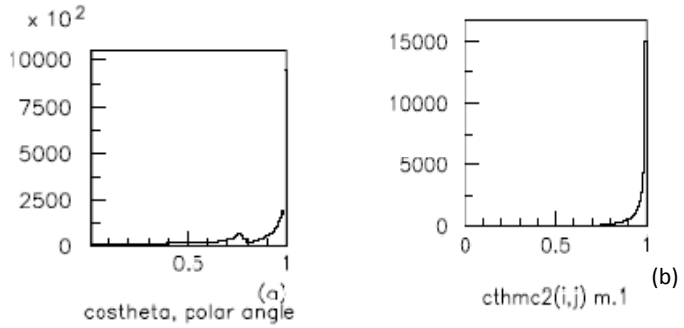

Figure 6.36 Cosine polar angles of K_L^0 candidates
(a) measured $\cos\theta$ and (b) $\cos\theta$ from Monte Carlo simulation.

6.2.4 Kinematic variables of neutron

Figure 6.37 gives the properties of reconstructed neutron candidates, with **Figure 6.37a** showing narrow width of $\delta_i = E_i - p_{zi}$ distribution for neutron candidates, indicating small difference between its energy and momentum in the z-component.

The centre of mass $W_{JB} = \sqrt{y_{JB}\, s}$, for the intermediate boson-proton for neutron candidates as in **Figure 6.37b** has a peak at about 25 GeV while the pseudorapidity is as in **Figure 6.37c**, indicating the highest production of neutron in the region $0 < \eta < 0.8$ in the forward region, as indicated by its momentum in z-component as in **Figure 6.35d.**

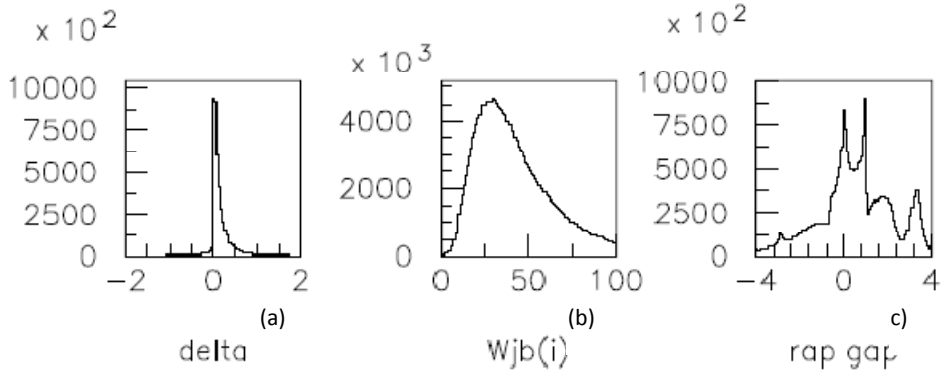

Figure 6.37 Properties of reconstructed neutron candidates (a) $\delta_i = E_i - p_{zi}$ (in GeV); (b) centre-of-mass $W_{JB} = \sqrt{y_{JB}\, s}$ for the intermediate boson-proton; (c) pseudorapidity η

6.2.5 Reconstructed mass of neutron

Figures 6.38a and **6.38b** gives the neutron mass constructed using selection criteria as described in **Section 5.1** of **Chapter 5**. The mass neutron candidates peak at 0.9GeV, which is in good agreement the invariant neutron mass of 0.939 GeV [35]. As in **Section 6.1.6**, the observed wide width peak is due to limited to only four variables available for neutron candidate selections i.e. polar angle θ, energy of object-*i* Zufos(4,i), and CAL and CAL EMC energies for neutral ZUFOs objects in the calorimeter that were not associated with any track.

Figure 6.38c gives the statistical error for the mass of neutron candidates, showing good standard deviation. In **Figure 6.38d,** the neutrons from Monte Carlo simulation is given, showing lower events then measured ones, perhaps to due to existence of background signals (and other neutron source from direct interactions) near the beampipe of the ZEUS detector.

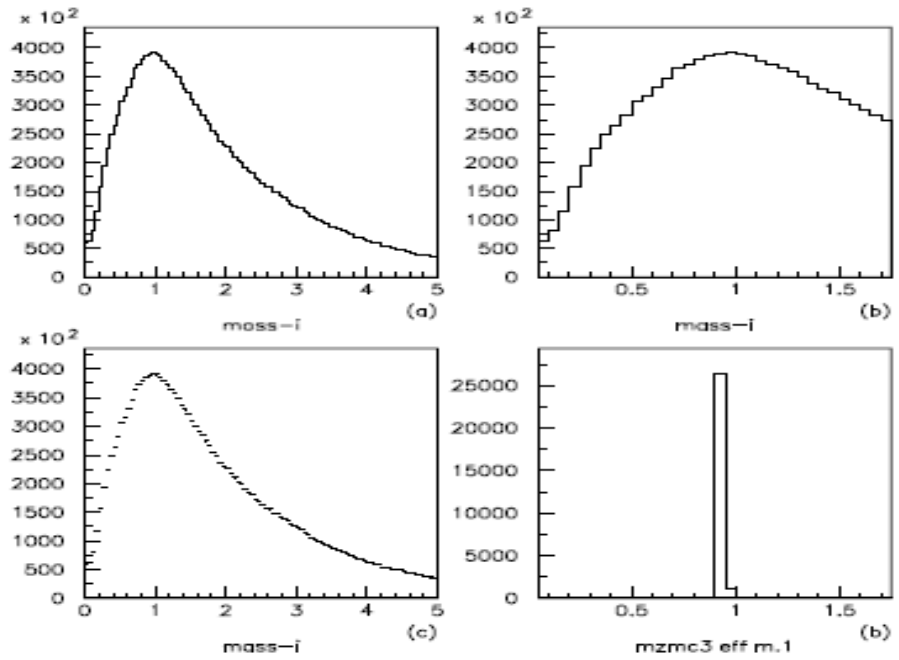

Figure 6.38 Reconstructed mass of neutron candidates in GeV (a) mass of neutron constructed from ZUFO objects not associated with any track; (b) an expansion of Figure (a); (c) neutron mass with errors; (d) neutron from Monte Carlo simulation. The invariant mass of neutron is 0.939GeV [35].

6.2.5.1 Neutron azimuthal angle

In **Figure 6.39,** two dimensional plot of neutron mass (in GeV) versus its polar angle θ is given, showing neutron direction at 0.2 radian (11.5^0) and consistent with observation in **Figure 6.36a.**

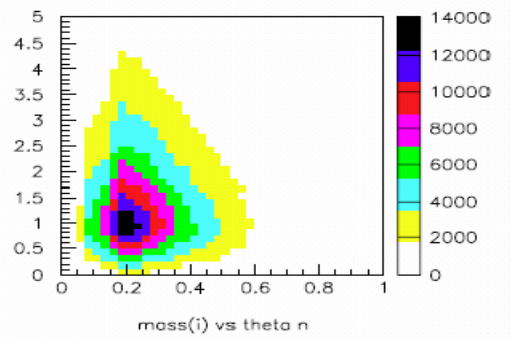

Figure 6.39 (a) Two dimensional plot of neutron mass (GeV) vs polar angle θ (rad) of neutron

6.2.5.2 Differential cross section of neutron

The differential cross section σ of neutron candidates with respect to its variable momentum p, was calculated using **Equation (5.6)** from **Section 6.1.6.1,** with integrated luminosity (2006/2007) of L =145.90pb^{-1} and B as the branching ratio 35.5% for $\Lambda \rightarrow n\,\pi^0$ decay channel.

Figure 6.40 compares the momentum of the measured (**Figure 6.40a)**, matched in magnitude and direction against the ones from generated from Monte Carlo (**Figure 6.40b**) and the corrected neutron candidates (**Figure 6.40c)**, while **Figure 6.41** shows the efficiency, purity and acceptance for momentum of neutron candidates. In these figures, except for **Figure 6.40c** that shows noise signal at momentum range <0.5GeV, the peaks occurred at ~3GeV, indicating that neutron production highest at around this peak.

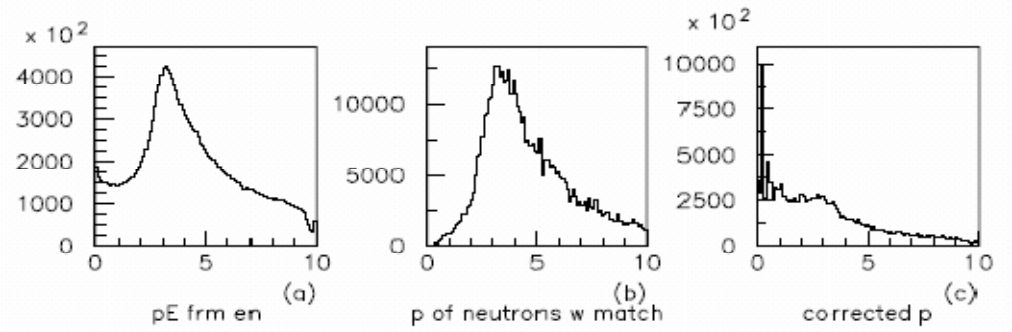

Figure 6.40 Comparison of momentum of neutron candidates (a) measured (b) matched in magnitude and direction against the ones from generated from Monte Carlo; (c) corrected

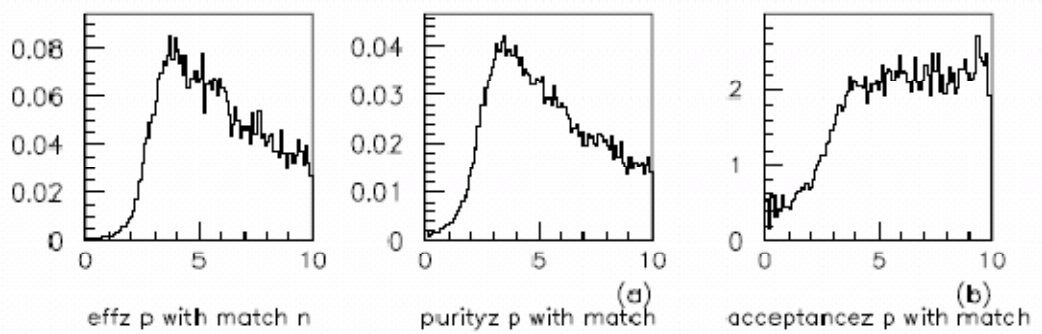

Figure 6.41 Comparison of (a) efficiency; (b) purity; (c) acceptance of momentum of neutron candidates

In **Figure 6.42**, the differential cross section with respect to momentum of neuron candidates showing similar in trend to the corrected momentum in **Figure 6.40(c),** a peak $d\sigma / dp$ ~5000pb/GeV at neutron energy ~3.5GeV. (At <0.5GeV range, there appeared to be noise signals in the differential cross section).

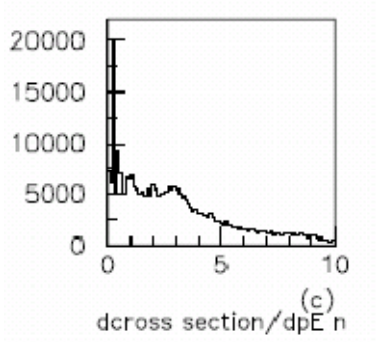

Figure 6.42 Differential cross section (in pb/GeV) of neutron candidates with respect to its measured momentum (in GeV)

6.2.6 Reconstruction of $\pi^0 \to \gamma\gamma$ candidates

To reconstruct the Λ mass from $\Lambda \to n\pi^0$, the π^0 candidates were reconstructed from $\gamma\gamma$ candidates from $\pi^0 \to \gamma\gamma$ decay channel using the selection criteria as given in **Section 5.4** of **Chapter 5**.

The momentum for the reconstructed $\gamma\gamma$ candidates is given in **Figure 6.43**, showing the z-component as having peak at 3GeV as in **Figure 6.43a**, as compare to the momentum of $\gamma\gamma$ candidates with a peak at 3.5GeV as in **Figure 6.43a,** indicating the tendency of $\gamma\gamma$ candidates to move in the forward direction.

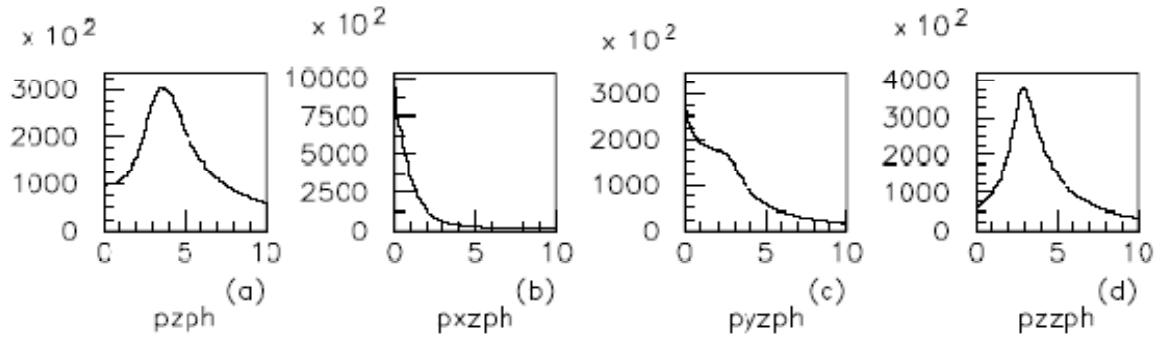

Figure 6.43 Reconstructed momentum (in GeV) of $\gamma\gamma$ candidates from $\pi^0 \to \gamma\gamma$ decay channel (a) momentum (b) momentum in x-direction (c) momentum in y-direction (d) momentum in z-direction

Figure 6.44a shows reconstructed mass of π^0 from $\pi^0 \to \gamma\gamma$ decay channel, while **Figure 6.44b** gives the energy of $\gamma\gamma$ candidates peaking at 3.5GeV. In **Figure 6.44c** the transverse energy of $\gamma\gamma$ is shown. **Figure 6.44a** shows the energy distribution of $\gamma\gamma$ candidates peaking at 3.5GeV, while the **Figure 6.44a** shows the peaking of polar angle $\theta \sim 14^0 (0.25 rad)$ of $\gamma\gamma$ candidates indicating the direction π^0 to be at $\theta \sim 14^0 (0.25 rad)$.

The reconstructed π^0 mass should be between $0.133 < \sqrt{E_{\gamma\gamma}^2 - p_{\lambda\gamma}^2} < 0.137\ GeV/c^2$ to narrow down the photon candidates that actually contributed to π^0 mass.

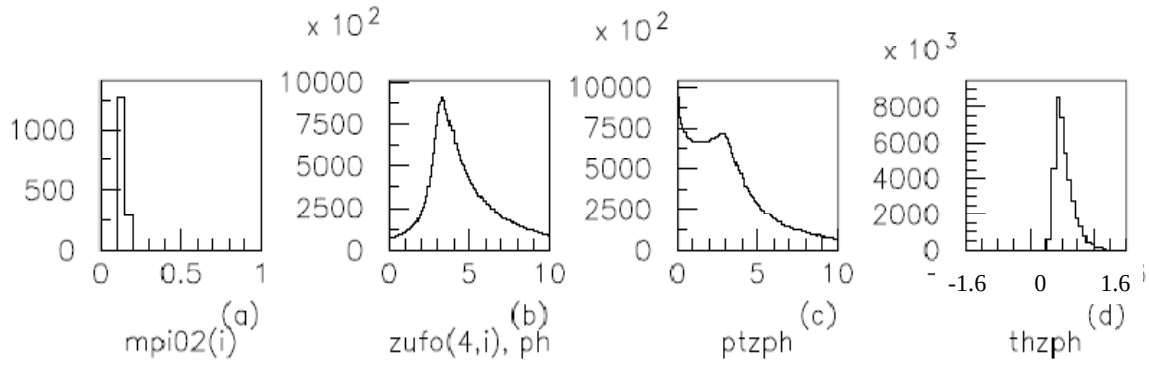

Figure 6.44 Properties of $\pi^0 \to \gamma\gamma$ candidates: (a) mass of π^0 in GeV narrowed to $0.133 < \sqrt{E_{\gamma\gamma}^2 - p_{\lambda\gamma}^2} < 0.137\ GeV/c^2$; (b) $\gamma\gamma$ energy (in GeV); (c) $\gamma\gamma$ transverse momentum in (GeV); (c) $\cos\theta$ polar angle of $\gamma\gamma$

6.2.7 Reconstruction of Λ

The reconstruction of Λ mass from $\Lambda \rightarrow n\,\pi^0$ decay channel was carried out using $m(\Lambda) \rightarrow m(n\,\pi^0)$. In **Section 6.2.5** of this chapter, the reconstruction of the neutron candidates is given, while in **Section 6.2.6** the result from event selection of π^0 using selection criteria as given in **Section 5.4** of **Chapter 5,** is given. From these event selections, the reconstruction of Λ mass from $\Lambda \rightarrow n\pi^0$ channel has been carried out, with the result as shown in **Figure 6.45.**

In **Figure 6.45a** and **6.45b,** the of Λ mass reconstructed from $\Lambda \rightarrow n\pi^0$ channel is shown, with peak at 1.1GeV which is in good agreement with the invariant mass 1.115 GeV [35]. The standard deviation of the reconstructed Λ mass has small error bars as given in **Figure 6.45c**, indicating good statistical sampling. For comparison purpose, the Λ mass from Monte Carlo simulation is also given in **Figure 6.45 (d).** The high entries of the measured Λ mass as compared with the simulated values indicate that the event selection needs further improvement.

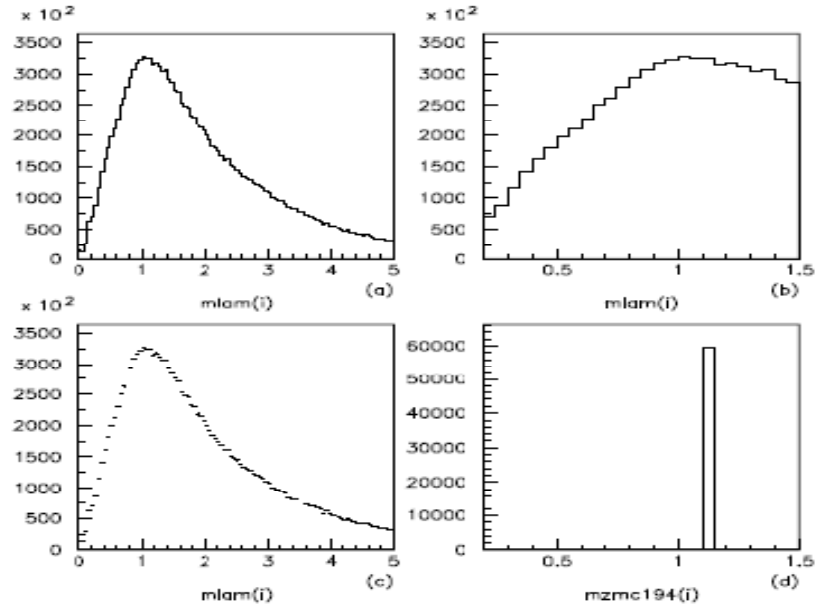

Figure 6.45 Reconstruction of Λ mass (in GeV) from $\Lambda \rightarrow n\pi^0$ channel (a) mass of Λ constructed from $m(\Lambda) \rightarrow m(n\,\pi^0)$ (b) an expansion of Figure (a); (c) Λ mass with errors (d) Λ from Monte Carlo simulation. The invariant mass of Λ is 1.115 GeV [35].

6.2.7.1 Differential cross section of Λ

Figure 6.46 compares momentum (in GeV) of Λ candidates, with **Figure 6.46a** giving the measured momentum, **Figure 6.46b** the corrected momentum and. **Figure 6.46c** simulated momentum from Monte Carlo that was matched in magnitude and direction against its measured momentum. In **Figure 6.46(a),** the momentum peaks at ~7GeV**,** with **Figure 6.46(b)** showing maximum at about the same value but with entries ~500.

In **Figure 6.47,** the efficiency, purity and acceptance of momentum of Λ candidates versus its energy (in GeV) are shown, with the efficiency and purity reaching maximum at ~ 7GeV.

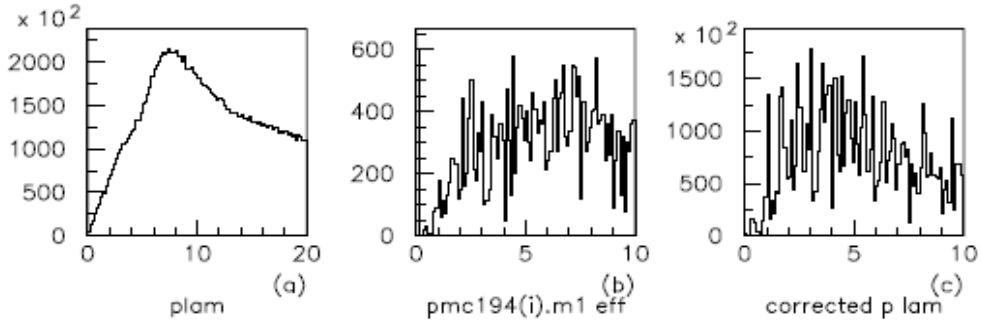

Figure 6.46 Comparison $\phi(1020)$ momentum (in GeV) (a) measured; (b) corrected; (c) simulated from Monte Carlo and matched in against measured momentum

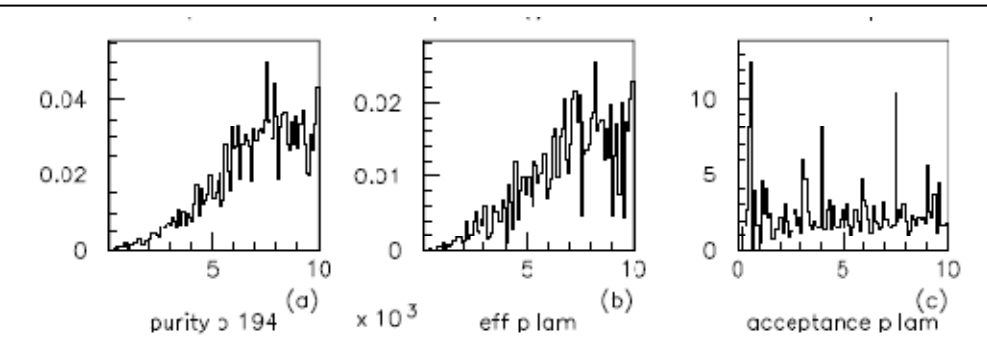

Figure 6.47 Comparison of (a) purity (b) efficiency; (c) acceptance of momentum of Λ candidates versus energy (in GeV)

The differential cross section σ with respect to the momentum p of Λ candidates is given in **Figure 6.48**, calculated using a standard bin-by-bin correction is given in **Equation (5.6)** of this chapter. In this figure, the maximum $d\sigma/dp$ ~15000pb/GeV at ~3.5GeV similar in trend to the corrected momentum in **Figure 6.46(c).**

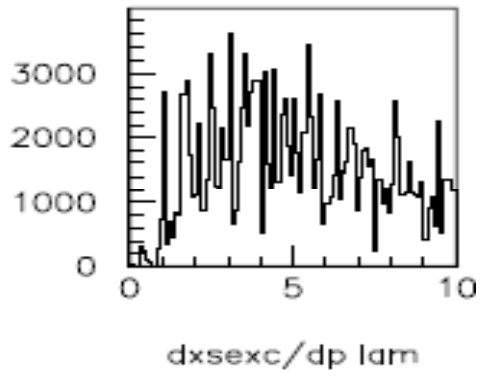

Figure 6.48 Differential cross section of neutron candidates with respect to its measured momentum (pb/GeV) vs its energy (in GeV).

6.4 Summary

In this chapter, the reconstruction of vector meson $\phi(1020)$ was carried out using the $\phi(1020) \rightarrow K_L^0 \, K_S^0$ channel and the reconstruction of baryon Λ through the decay channel $\Lambda \rightarrow n \, \pi^0$.

Using the selection criteria in **Chapter 5**, the candidates of long live neutral hadrons K_L^0 and neutron that reached the hadronic calorimeter (HACs) of the ZEUS detector was selected from the uncharged ZUFO objects not associated with any track that formed islands of energy deposits in the HACs.

In both K_L^0 and neutron, their momentum momentums were prominent in the z-direction than in x and y direction, more so for neutron. For K_L^0 , the energy deposited in the calorimeter peaked at 5GeV, while for neutron the energy peaked at 6GeV. The small energy range of K_L^0 and neutron that reached the calorimeter suggest that their production were from on-mass-shell hadrons. In the string-fragmentation scheme, a $q\bar{q}$ pair may be created from the vacuum when the string between two color partons provided that the invariant mass of the string pieces exceed on-mass-shell hadrons.

The Vector Meson Dominance (VDM), as described in **Section 2.6**, postulated a scattering of virtual photon from the irradiation of incoming electron, could acquire a hadronic structure that allows it to fluctuate into the hadron target during *ep* interaction, and coupled to a to a bound $q\bar{q}$ state that have the same quantum number as the photon and caused the vector meson (ρ, ω, ϕ) fluctuations, and scattering elastically off the incoming proton via a pomeron exchange. The SU(3) in the proton structure that transformed the gluons in the proton into

hadron $\phi(1020)$ with an $s\bar{s}$ state when virtual photon coupled to a bound $q\bar{q}$ state of the proton was modeled by Color Dipole Moment (CDM), that assumed the $q\bar{q}$ pair as as radiation of color dipole between the quark q and antiquark $\bar{q}$ pair. In case of $\phi(1020) \rightarrow K_L^0\ K_S^0$ decay channel, the state of $s\bar{s}$ in $\phi(1020)$ is partially retained in K_L^0 ($d\bar{s}$) with momentum higher than K_S^0 ($d\bar{s}$).

In the Lund String Model as given in Section 2.4, the hadronisation of quarks and gluons to form hadrons during *ep* interacton involves the fragmentation of color flux sring-like gluons that are binding the quarks and antiquarks ($q\bar{q}$) in hadrons. Fragmentation of hadron Λ with state uds into n (udd) and π^0 ($u\bar{d}$) is possible if the energy stored in the string is sufficient enough as when two color partons move apart, to form a $q\bar{q}$ pair from the vacuum.

In case of decay $\Lambda \rightarrow n\,\pi^0$ channel, the conservation of strangeness number S = -1 through where charges of both mother and decay products were conserved. Using the selection criteria as given in **Section 5.1**, the momentum of neutron peaked at ~3.0GeV while the momentum of $\gamma\gamma$ from π^0 decay peaked at ~3.8GeV indicate that the production of n and π^0 as a result from on-mass-shell hadrons.